— 22 —

Microchannel plates for photon detection and imaging in space

J. Gethyn Timothy[I]

Abstract

This chapter describes the development of the continuous-dynode electron multiplier and its evolution into the microchannel plate (MCP). The fabrication procedures for MCPs are described and the performance characteristics of MCPs and MCP stacks are enumerated. The configurations and performances of imaging MCP electronic readout systems currently in use in space instruments are described in detail. The unique capabilities of MCP electronic systems for fast timing and for time-tag imaging are listed. Finally, the prospects for the development of the next generation of MCPs are briefly outlined.

Background

The conventional photomultiplier tube (PMT), invented in the 1930s, employs a photocathode to convert the detected photon to a photoelectron, and a discrete dynode electron multiplier to amplify the charge of the single photoelectron to the level that can be recorded by commercial electron circuits. Still in wide use today, a number of dynode configurations, e.g., as shown in Figure 22.1, have been developed for PMTs. The discrete dynode electron multiplier is not optimized for space observations. First, the dynode structure has to be ruggedized in order to survive the launch environment. Second, the complex arrangement of the high-voltage dynode electronics does not permit compact packaging. Third, and most important, most of the efficient secondary electron emitting materials used to coat the dynodes cannot survive exposure to air. This prevents the use of the multiplier in an open structure configuration in the windowless region at extreme ultraviolet (EUV) wavelengths below about 116 nm. One exception was the use of a multiplier with high work function beryllium-copper dynodes to study EUV radiation at wavelengths between 10 nm and 80 nm (Piore et al 1952).

The concept of a continuous-dynode electron multiplier was first proposed by Farnsworth (1930), but the fabrication of practical devices was delayed until

[I]Nightsen, Inc., Tiverton RI, USA

M.C.E. Huber et al. (eds.), *Observing Photons in Space: A Guide to Experimental Space Astronomy*, ISSI Scientific Report Series 9, DOI 10.1007/978-1-4614-7804-1_22,

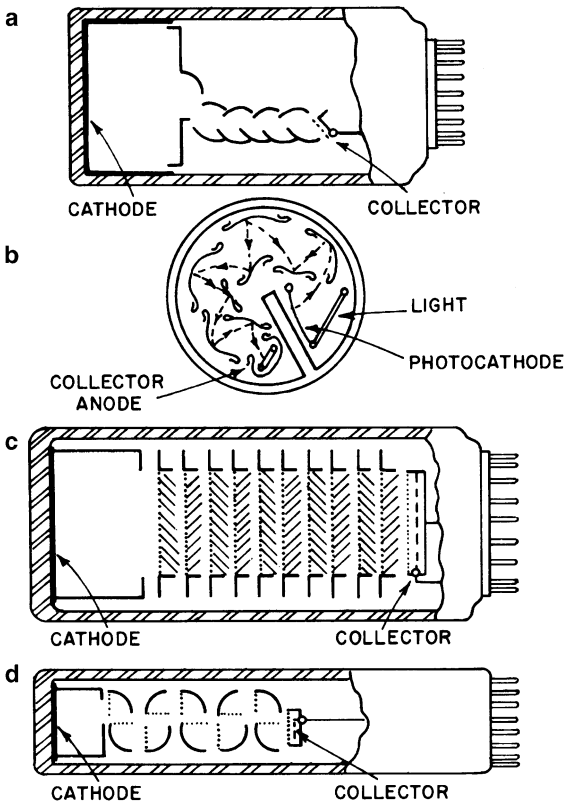

Figure 22.1: Dynode configurations for PMTs: a) linear focused; b) squirrel cage; c) venetian blind; d) box-and-grid (from Young 1974).

advances in the understanding of the processes of secondary electron emission and in the development of high surface resistance glasses had been made in the 1960s. The first practical continuous-dynode multiplier was the Bendix magnetic electron multiplier (MEM) (Heroux and Hinteregger 1960; Timothy et al 1967). Macar et al (1970) have given a detailed analysis of the electron multiplication process in the MEM.

As shown in Timothy et al (1967), the MEM consists of two glass strips with baked-on high-resistance tin oxide and antimony coatings surrounded by a series of magnets. An electrostatic field is established along the strips by four high-voltage connections. A photoelectron, formed on the opaque photocathode, is accelerated in a trochoidal path along the dynode strip, causing the emission of secondary electrons at each impact. Gains of order 10^6 were obtained with applied potentials of the order of 2000 V, and the MEM operating characteristics remained stable with exposure to the ambient atmosphere. Relative detection efficiencies of up to 5 % at 60 nm were obtained with opaque tungsten photocathodes.

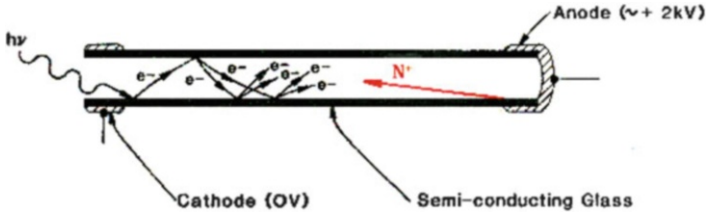

Figure 22.2: Schematic of the straight-geometry channel electron multiplier (CEM). Positive ion feedback is shown.

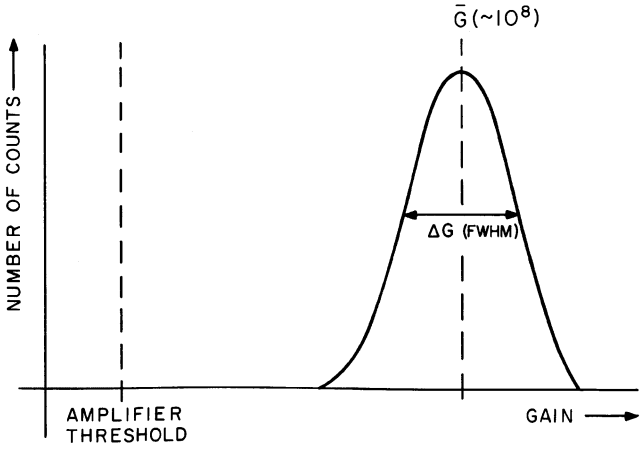

Figure 22.3: Schematic of saturated output pulse height distribution for a curved-channel CEM.

A major advance in the development of continuous-dynode electron multipliers took place in the 1960s with the production of high-resistance surfaces on lead glasses through the process of high-temperature $\approx 300\,^{\circ}$C to $\approx 450\,^{\circ}$C reduction in a hydrogen atmosphere (Blodgett 1951). This led to the independent development of the continuous channel electron multiplier (CEM) by Oschepkov et al (1960) in the Soviet Union, by Goodrich and Wiley (1962) at the Bendix Research Laboratories in the USA, and by Adams and Manley (1966) at the Mullard Laboratories in the United Kingdom and at the Laboratoires d'Electronique et de Physique Appliquée (LEP) in France (both part of the Philips Corporation). The mode-of-operation of the CEM is shown in Figure 22.2. The multiplier is operated under vacuum with a high voltage established along the channel. A high-energy photon or charged particle striking the wall of the channel releases an electron with some initial energy that is accelerated along the channel axis, drifting across to strike the wall with sufficient energy to release secondary electrons. This process is repeated many times with a final output pulse containing up to 10^8 electrons. As the voltage along the channel is increased, the energy of the electrons striking the wall will increase, but the total number of impacts will decrease. It can thus be expected that the electron

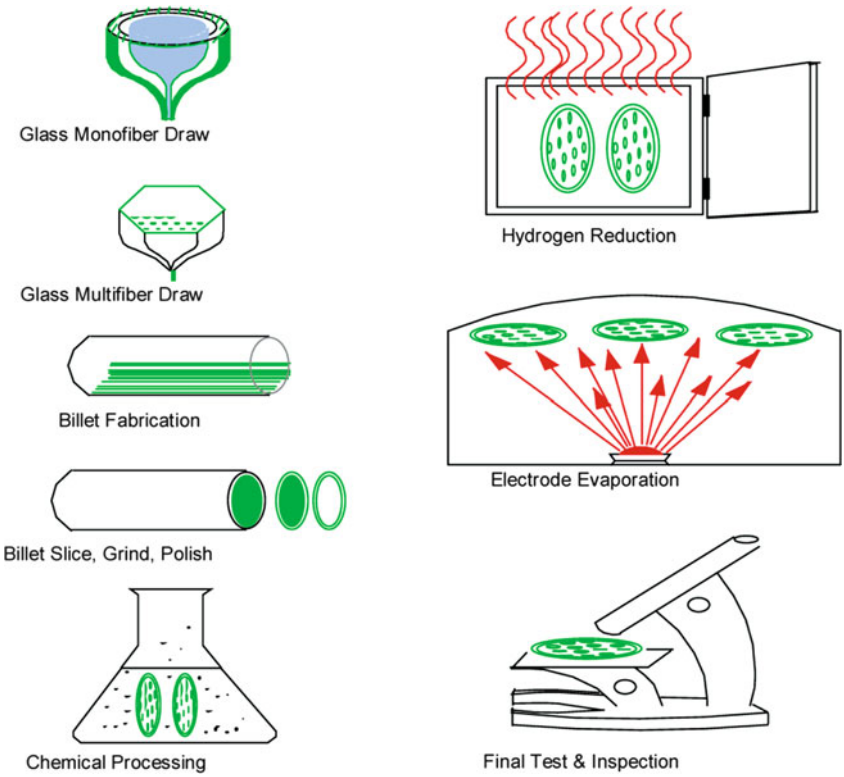

Figure 22.4: Process for fabricating MCPs using etchable core glass (from Laprade et al 1997).

gain (amplification) will increase to a maximum value and then start to decrease. Adams and Manley (1966) derived an expression showing the dependence of the gain on the applied voltage as:

$$G = \left(\frac{K\, V_0^2}{4\, V\, \alpha^2} \right)^{4V\alpha^2/V_0} \quad , \tag{22.1}$$

where G is the gain, V_0 is the energy gained by an electron traversing the applied potential difference, V is the initial energy of the secondary electron, α is the length-to-diameter ratio of the channel, K is a constant from the relation $\partial \approx KV_c$, with ∂ the secondary emission coefficient and V_c the collision energy.

However, the experimental gain curve does not show a maximum, as predicted by the model, but continues to much higher gain levels and then starts to saturate. This is because, first, the secondary electrons are not all emitted orthogonally, and, second and more important, the gain is enhanced by ion feedback. As shown in the schematic in Figure 22.2, the voltage that accelerates the electrons down the channel can also accelerate a positive ion, caused by the impact of an electron with

a residual gas molecule, back to the input where it can impact the wall and restart the gain process. The level of ion feedback depends both on the ambient pressure and the level of the applied voltage.

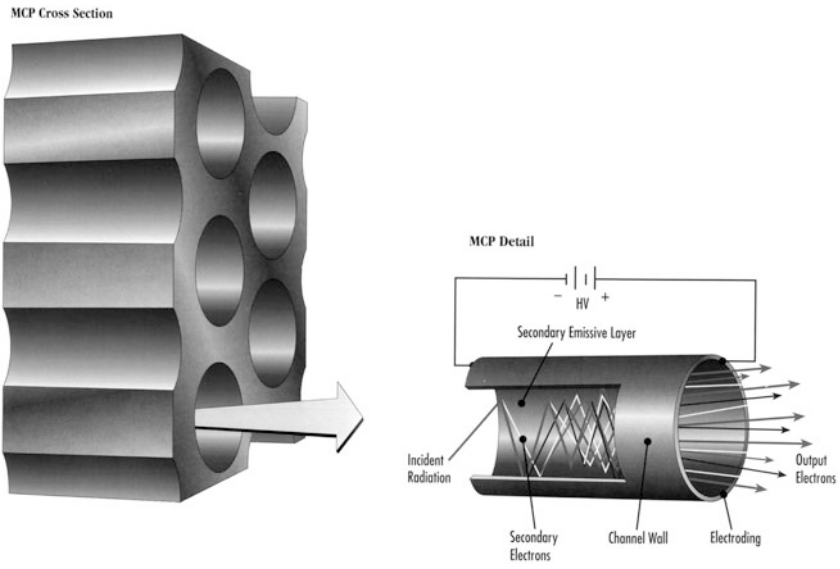

Figure 22.5: Schematic showing mode-of-operation of the MCP (from GEOC, now Photonis USA).

The feedback of positive ions can be prevented by curving the channel, forcing the ions to impact the wall in a short distance compared with the total channel length. Evans (1965) calculated the degree of curvature required to effectively suppress ion feedback and permit stable operation of a CEM at gain levels high enough to permit single photoelectron detection. Eschard and Manley (1971) have reviewed the differences in the performance characteristics of the different types of CEM. The curved-channel CEM is effectively immune to ion feedback when operated under high vacuum at pressures less than about 1.3×10^{-5} hPa. Further, when operated at high voltages (> 2 kV), the distribution of output pulses changes from a negative exponential form to the quasi-Gaussian saturated form shown in Figure 22.3. Evans (1965) has suggested that the saturation is caused by the distortion of the potential gradient within the channel by the deposition of positive charge on the walls at the output end. A CEM with an internal channel diameter of order 1.0 mm and a length-to-diameter ratio of order 100:1 can produce a modal gain $> 10^8$ and a relative resolution (ΔG or R) in the range 35 % to 60 %. The CEM provides a stable photometric response when operated in gain saturation (Timothy and Lapson 1974), and has been used with great success in the open-structure mode to study EUV radiation on a number of sounding rockets and orbital space missions (see, for example, Timothy et al 1975 and Reeves et al 1977).

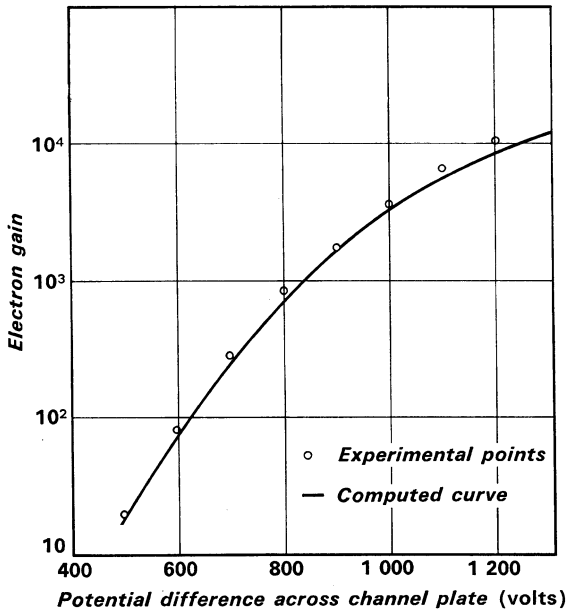

Figure 22.6: Measured and computed gain as functions of voltage for an MCP with a channel length-to-diameter ratio of 40:1 (from Guest 1971).

Microchannel plates

It is important to note from Equation 22.1 that the fundamental electrical characteristics of the CEM depend on the length-to-diameter ratio α of the channel and not on the absolute physical dimensions. The size of the channel can thus be reduced to the limit set by the available glass technology. Further, many channels can be bonded together to produce a detector with an image recording capability. The first microchannel plates (MCP) were assembled by bonding together about five thousand CEMs with ≈ 100 µm channel diameters at the Bendix Research Laboratories (Wiley and Hendee 1962).[1] These early efforts were rapidly replaced by the application of fiber draw techniques, as described by Washington et al (1971).

The first processes utilized the drawing of hollow fibers, or metal core fibers. Subsequently, the process was modified to utilize the drawing of fibers with etchable glass cores. This is the process used to this day in Europe, the US (Wiza 1979), and in the rest of the world. The process sequence is shown in Figure 22.4. A two-part billet, several centimetres in diameter, consisting of an etchable glass

[1]The progression of MCP manufacturers in Europe and the USA requires clarification in order to avoid confusion. In Europe, Philips closed the Mullard MCP fabrication facility in the UK in 1988 and moved MCP fabrication to Photonis in Brive, France. Photonis became independent of Philips in 1998. In the USA, Bendix Research Laboratories in Ann Arbor, Michigan transferred to Galileo Electro-Optics Corporation (GEOC), Sturbridge, Massachusetts in 1972. In 1999 GEOC was purchased by Burle Industries and became Burle Electro Optics. In 2005 Burle Electro Optics was purchased by Photonis and is currently Photonis USA.

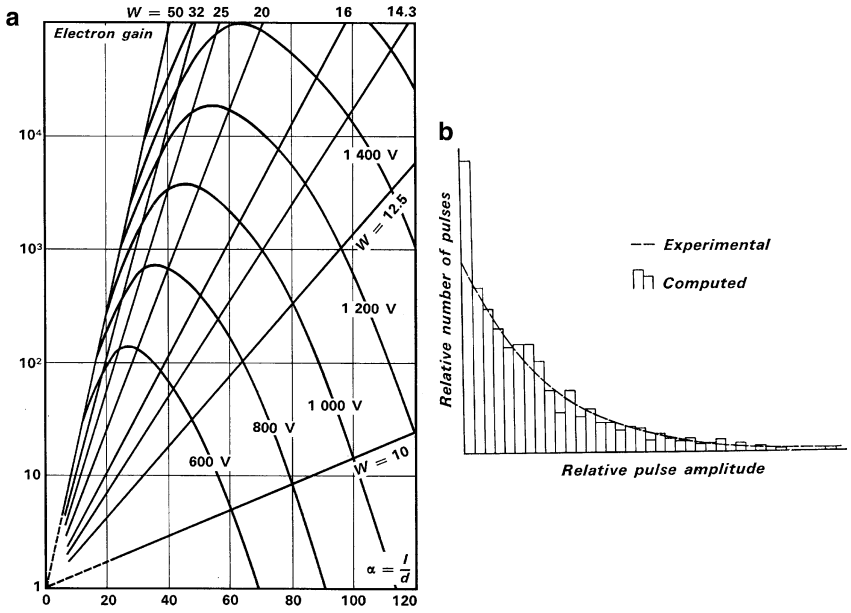

Figure 22.7: a) Universal gain curves for an MCP. $W = V/\alpha$ (from Guest 1971). b) Measured and computed output pulse height distributions for a straight-channel MCP operated at low gain (from Guest 1971).

core surrounded by a proprietary lead glass cladding is drawn down to a single fiber. About 3×10^3 fibers are then fused together to form a hexagonal multi-fiber billet. This billet is then drawn down again to form hexagonal multi-fibers. These multi-fibers are then fused together to create the MCP boule or billet. The MCP wafers are then produced from this boule by slicing, grinding and polishing. The next steps are the etching out of the core glass and chemical processing of the resulting lead glass interior surfaces of the channels. The semi-conducting surfaces of the channels are then produced by heating the MCP wafer in a reducing atmosphere of hydrogen to yield a very thin free lead layer. Finally the input and output faces of the MCP wafer are electroded, typically with nichrome or inconel, to provide electrical contacts. The basic structure and mode-of-operation of the MCP is shown in Figure 22.5. Great care must be taken with the fusion of the hexagonal multi-fibers in order to avoid channel distortions at the interfaces. Distortion of the channels at the multi-fiber interfaces can change the length-to-diameter ratio and the gain at a given voltage. This leads to a hexagonal pattern in the flat-field response known as "chicken wire". Recent advances in reducing multi-fiber edge effects have been reviewed by Siegmund et al (2007). Most MCPs have a planar format, although MCPs with a steep curvature to match the focal planes of optical instruments have also been successfully fabricated (see, for example, Siegmund et al 1990).

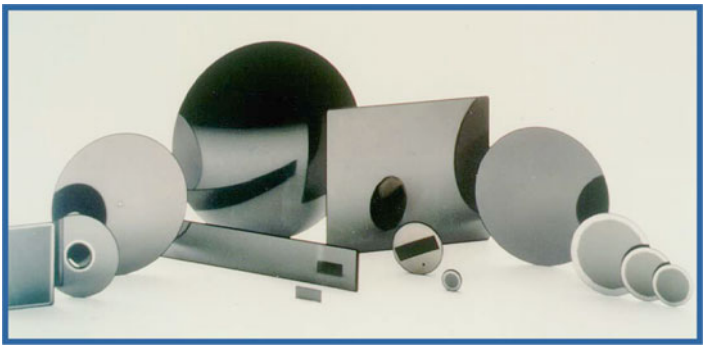

Figure 22.8: Different MCP configurations (from the Burle Electro-Optics, now Photonis USA, catalog). Diameters of the circular MCPs range from ≈18 mm to ≈125 mm.

MCP performance characteristics

The expression for the CEM gain (Equation 22.1) has been further refined by Guest (1971) in a computer model for a channel whose performance is not modified by space charge and wall charging effects, i.e., at gain less than 10^5. This model is in good agreement with the experimental data, as shown in Figure 22.6. Most importantly, the Guest model allows the calculation of a set of universal gain curves for an MCP, as shown in Figure 22.7a. It can be seen that there is an optimum combination of applied voltage V and length-to-diameter ratio α where slight variations in the length-to-diameter ratio do not significantly affect the gain. Specifically for the optimum length-to-diameter ratio, the ratio W is:

$$W = \frac{V}{\alpha} \approx 22.5 \quad . \tag{22.2}$$

Channel length-to-diameter ratios in the range 40:1 to 60:1 are accordingly used in image intensifier tubes at operating voltages between 1000 V and 1200 V (see, for example, Csorba 1980). At these voltages the MCP produces a negative exponential output pulse height distribution, with most of the pulses at low amplitudes, as shown in Figure 22.7b. This is clearly not optimum for a stable photometric response as a slight reduction in the gain will cause a number of pulses to be lost below the threshold of the electronics, significantly reducing the detective quantum efficiency (DQE). The development of MCPs has been inexorably linked with the development of military night-vision image tubes. Currently MCPs are available from a number of vendors with channel diameters ranging from 25 µm down to 2 µm. Typically the open-area ratio of the channels is of the order of 60 % of the area of the plate. The diameters of circular-format MCPs range from ≈18 mm to ≈150 mm. MCPs can be obtained in rectangular formats, with holes in the centre for ion detection applications, and with active areas configured to match specific readout systems, moreover with solid rims or rimless (see Figure 22.8). Catalogs of MCP configurations can be obtained from, amongst others, `www.photonis.com`, and `www.sales.hamamatsu.com`. The best MCPs for high-resolution imaging are

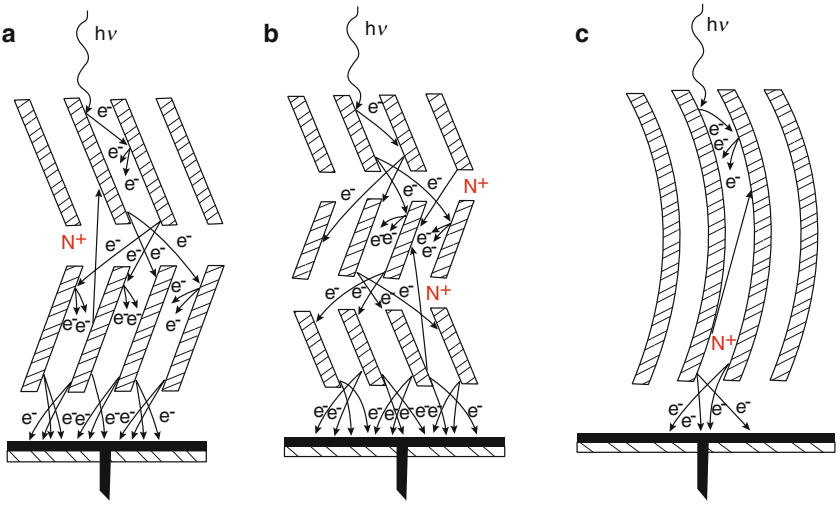

Figure 22.9: High-gain MCP configurations. a) Chevron MCP stack. b) Z-plate MCP stack. c) Curved-channel C-plate MCP.

the 18 mm, 25 mm, and 40 mm formats, since these are fabricated using boule fusion techniques rather than the block fusion techniques employed for larger formats. Typically, the channels in these MCPs have bias angles with respect to the input face of the plate in the range 0° to 20°.

The maximum gain that can be realized without significant ion feedback in a straight-channel MCP is of the order 10^3 to 10^4. These gain levels are not high enough for electronic readout systems. In order to obtain higher gains without ion feedback, alternative MCP configurations must be employed. Three types of high-gain MCP configurations are currently in use, as shown in Figure 22.9. The first type is the "chevron" MCP stack shown in Figure 22.9a. The performance characteristics of this configuration have been reported by Wiza (1979). In the chevron MCP stack two straight-channel MCPs with channel bias angles typically in the range from 8° to 10° are mounted in sequence with the bias angles set so that positive ions are trapped at the interface between the two MCPs. An improvement on the chevron MCP stack is the "Z-plate" MCP stack shown in Figure 22.9b. In the "Z-stack" three MCPs with matched resistances are mounted in a butt-faced configuration with the positive ions trapped at the two MCP interfaces (see, for example, Siegmund et al 1994). The Z-stack provides a significantly better reduction of ion feedback than the chevron MCP stack and is the most-used high-gain MCP configuration at this time.

The third type of high-gain MCP configuration is the curved-channel MCP or "C-plate" MCP shown in Figure 22.9c. The channels in this MCP are curved in a manner analogous to that of the curved-channel CEM. Washington (1971) stated that for a curvature sufficient to mask the output 30 % of the channel would be required to effectively suppress ion feedback to the channel input. The first curved-channel MCPs with the output end strongly curved ("J-plates") were

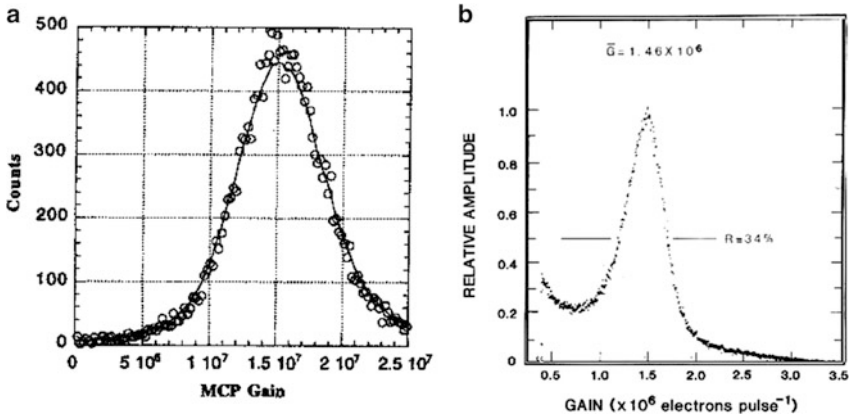

Figure 22.10: High-gain MCP output pulse-height distributions. a) Z-plate MCP stack (from Siegmund et al 1994). b) C-plate MCP (from Timothy 1981).

fabricated by LEP in France and Mullard in the UK (see, for example, Boutot et al 1974). Typical length-to-diameter ratios for C-plate MCPs lie in the range 80:1 to 120:1. A single C-plate MCP can be operated at high gain $> 10^6$.

C-plate MCPs with, first, J-sections, and later C-sections were successfully fabricated in the US by GEOC starting in the early 1970s (Timothy and Bybee 1977a; Timothy 1981).

Typical relative resolutions for chevron MCP stacks range from ≈ 120 % to ≈ 60 % at gains around 10^7 and for Z-plate MCP stacks from ≈ 60 % to ≈ 35 % at gains around 10^8. A single C-plate MCP produces resolutions ranging from ≈ 50 % to ≈ 35 % at gains around 10^6. Examples of the saturated output pulse height distributions from a Z-stack MCP and a C-plate MCP are shown in Figure 22.10. The single C-plate MCP is the mechanically most stable of the three configurations, and produces the least spreading of the output charge cloud. It also produces the lowest level of ion feedback. However, C-plate MCPs have proved extremely difficult to manufacture. Corbett et al (1992) have described some of the more critical problems. The result is that C-plates have only been produced for space missions with adequate resources, such as the *HST*, and C-plates are not commercially available at this time. The best high-gain MCP configuration available at this time is the Z-stack (Siegmund et al 1995).

Image intensifier tubes

Thousands of MCPs are produced each month for use in image intensifier tubes for military and civilian night-vision applications. Csorba (1985b) has described the different types of image intensifier tube developed to date. The development of the second generation (Gen II) wafer tube (see Figure 22.11), employing an MCP to amplify the internal electron current, revolutionized passive night vision. Earlier tube configurations (Gen 0 and Gen I), which employed a photocathode

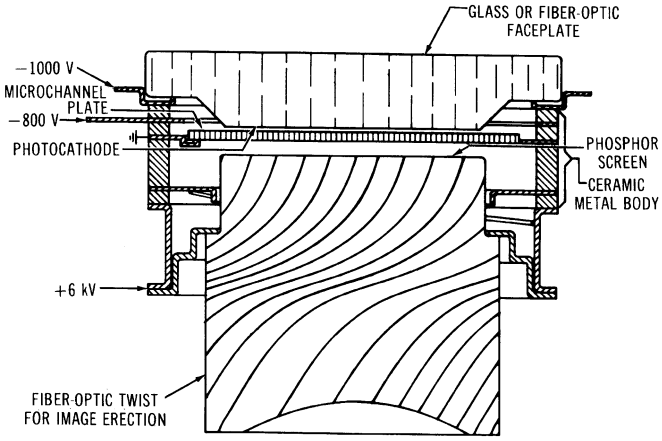

Figure 22.11: Structure of Generation II night-vision wafer tube employing an MCP intensifier (from Csorba 1985a).

and accelerated the photoelectron directly to a phosphor, yielded amplifications of the order of 1000. In contrast, the Gen II wafer tube with an MCP provides amplifications of the order of 10 000 to 20 000.

The emphasis in night vision is on the response to red and near-infrared wavelengths, since starlight has a predominantly red spectrum. For many years photocathode materials were developed empirically by trial and error, as described by Sommer (1980). The Cs-Na-K-Sb trialkali (S-20) multialkali photocathode was found to have the best red response and is typically used in the Gen II tubes. In the 1970s negative-affinity photocathodes were developed from physical principles (Spicer 1975). In particular, the GaAs photocathode, doped with extremely thin layers of Cs and O, was found to have an extremely high response at red and near-infrared wavelengths. This photocathode is used in the state-of-the-art Gen III image tube that produces amplifications of the order 30 000 to 50 000.

Other photocathode materials can be employed in the image intensifier tubes for scientific applications. At shorter wavelengths the S-11 bialkali photocathode provides a strong blue response, and at vacuum ultraviolet (VUV) wavelengths the Cs-Te photocathode provides a strong response down to about 170 nm, with a high degree of solar blindness at wavelengths longer than about 350 nm. All of these semi-transparent photocathode materials must be remotely processed in order not to contaminate the MCP with Cs, and must be mounted on a window in proximity focus with the MCP input.

At wavelengths below about 170 nm, high work function opaque photocathode materials are available which can be deposited directly on the front face of the MCP. Opaque CsI deposited on the front face of the MCP provides a strong response at wavelengths below about 180 nm. However, CsI is hygroscopic and the quantum efficiency degrades on exposure to air. The DQEs of image tubes with MgF_2 windows and semi-transparent Cs-Te and opaque CsI photocathodes are shown in Figure 22.12.

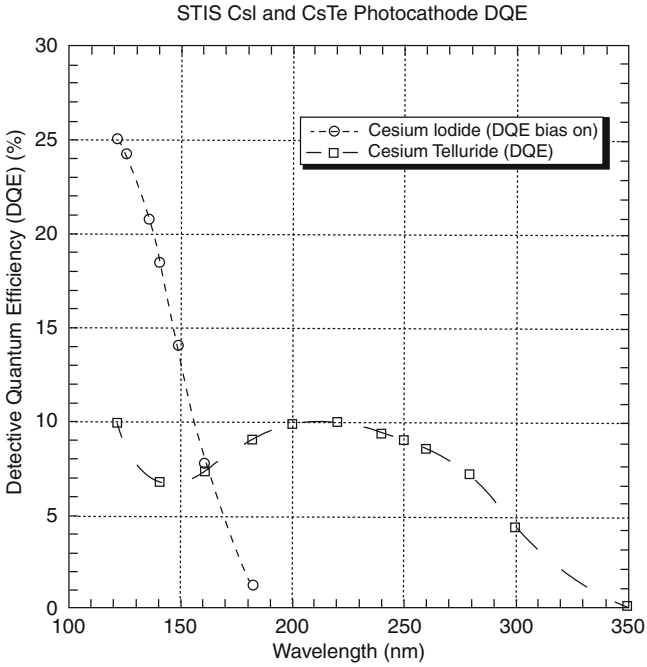

Figure 22.12: DQEs of image tubes developed for the Space Telescope Imaging Spectrograph (STIS) with MgF_2 windows and, respectively, a semi-transparent Cs-Te photocathode and an opaque CsI photocathode.

At shorter wavelengths higher work function photocathode materials are available which are stable on exposure to air. Materials such as opaque MgF_2, KBr, RbBr, and CsBr, deposited on the front face of an MCP provide high DQEs at wavelengths progressively shorter than about 150 nm (Siegmund et al 1987; Tremsin and Siegmund 2005).

The output phosphor screen in a typical night-vision tube is a P-20, which produces a green image to which the human eye is most responsive. Other phosphor screens are available, as described by Csorba (1985a).

Electronic readout systems for the MCP image intensifier tubes are required for use in space. The modifications to the tubes required to use CCD or CMOS-APS electronic readout systems are described in Chapter 25 (Schühle 2013). Direct electronic readout systems for high-gain MCPs are described in the next section of this chapter.

Electronic readout systems

Three classes of electronic readout systems are available for use with high-gain MCPs. The first class is the discrete anode arrays in which each pixel electrode is connected to its own amplifier/discriminator and counting circuit. The second class

is the analog readout arrays, which employ charge-division or timing-discrimination techniques to determine the coordinates of the detected photon. The third class is the digital readout arrays, which employ specially configured anodes to determine the coordinates of the detected photon.

In the discrete anode readout arrays the spatial location and resolution are defined by the geometry of the pixel electrodes, as shown in Figure 22.13. As an example, a special double linear array was developed for the spectrometer on the *SPARTAN 201* mission (Kohl et al 1994), as shown in Figure 22.14. Linear arrays of 1×160 pixels and area arrays of 10×10 pixels have been used with 25 mm format and 40 mm format high-gain MCPs. Discrete anode MCP photomultiplier tubes are commercially available (see, for example, `www.photonis.com`). There are local and global dynamic range limitations with all three classes of electronic readout systems for high-gain MCPs. The local dynamic range is set by the output count rate capability of the MCP. The modal gain will start to fall when the avalanche current reaches about 10 % to 20 % of the wall current, as shown in Figure 22.15. Reducing the resistance of the channels can increase the dynamic range. A C-plate MCP with the characteristics of that shown in Figure 22.15, but with a resistance of only 26 MΩ, produced a linear resistance to output count rates greater than 10^5 mm^{-2} s^{-1}. Small-pore MCPs will typically have the largest dynamic range, albeit at slightly lower gain levels.

Similar gain reductions are observed with chevron and Z-stack MCPs, but are mitigated by charge spreading into adjacent channels in the second and third MCPs. This however leads to a scene-dependent dynamic range reduction when observing bright objects covering many channels in the first MCP, because of the overlapping charge clouds. Wilhelm et al (1997) have discussed this effect in the context of observing strong solar emission lines with the SUMER instrument on the *SOHO* mission (see Chapter 5, Timothy et al 2013). There is a limit to the conductivity of an MCP, since the lead glass has a negative temperature coefficient of resistance (see Timothy 1981). Too low a resistance will result in thermal runaway from ohmic heating, leading to the destruction of the MCP.

The number of pixels in a discrete anode array is limited to several hundred both by the connector technology of the tubes and the complexity and power requirements of the associated electronics. Much larger array formats are required for imaging and spectroscopy, particularly in space at wavelengths below ≈ 300 nm. A series of analog and digital systems for encoding the position of the detected photon have been developed to meet this requirement.

The first of the analog systems is the resistive anode encoder (RAE) or RANICON (Lampton and Paresce 1974; Wiza 1979). The readout array is a resistive anode with readouts at either end for a linear array, and at each corner for an area array. The position of the detected photon is determined by the proportion of the charge collected at each end, or by pulse rise-time discrimination. In order to avoid the inherent distortions in the two-dimensional RAE, a circular arc-terminated resistive anode is employed, as described by Lampton and Carlson (1979). Early RANICONs yielded formats of ≈ 100 × 100 pixels, pixel dimensions of order 100 μm or better, and total count rates of a few hundred counts per second with MCP gains in excess of about 5×10^6. Later, PHOTICON tubes with bialkali, trialkali, or GaAs photocathodes, and a stack of five MCPs produced formats of

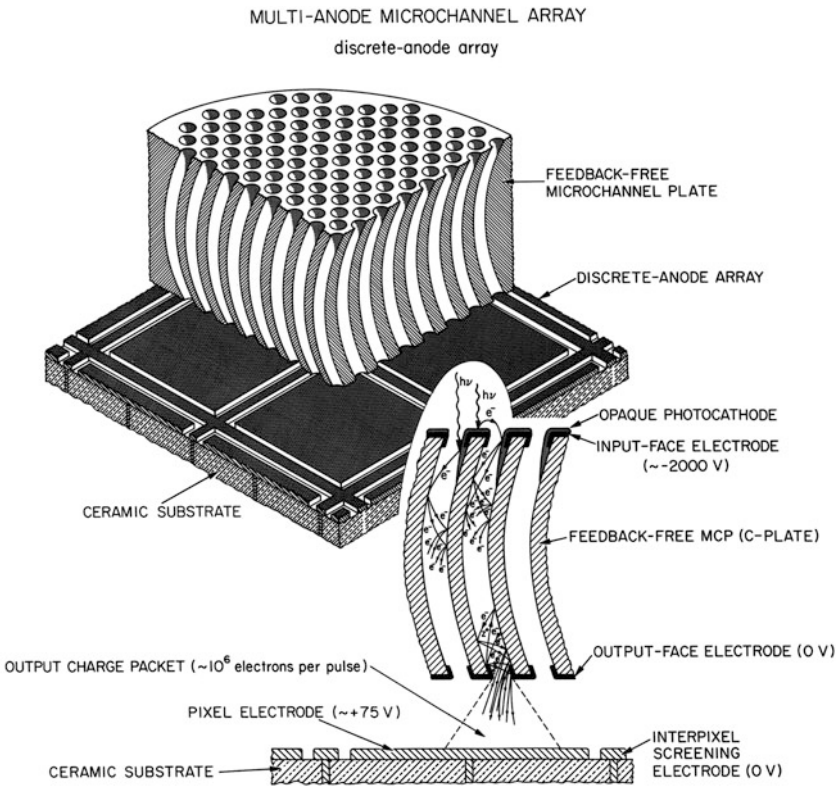

Figure 22.13: Schematic of a discrete anode MCP readout array. A C-plate is shown but the array can also employ chevron or Z-stack MCPs (from Timothy and Bybee 1977b).

1024×1024 pixels, pixel dimensions of ≈ 70 μm^2, and total count rates of a few hundred kilohertz (Clampin and Paresce 1989). The RAE was used as the soft X-ray detector (Mason et al 1984) on the *EXOSAT* mission (De Korte et al 1981).

An analog readout array that eliminates the inherent resistive noise in the RANICON readout array is the wedge-and-strip array (WSA) (Martin et al 1981). A four-electrode WSA is shown in Figure 22.16. Three and five electrode patterns can also be used. Siegmund et al (1986) have described the operating characteristics of the WSA readout systems. Large-format WSA detectors with more than 512×512 pixels have been successfully used on the *EUVE* mission (see Chapter 5 of this volume). Siegmund et al (1984) have described the configuration of these detectors, and Vallerga et al (1994) have described the long-term on-orbit performance. Siegmund et al (1985) have described the performance characteristics of the large-format Z-stack MCPs used with these detectors.

A variation of the WSA, namely the one-dimensional spiral anode (SPAN) detector (Breeveld et al 1992) was used in the CDS instrument on the *SOHO* mission (see Chapter 5 of this volume).

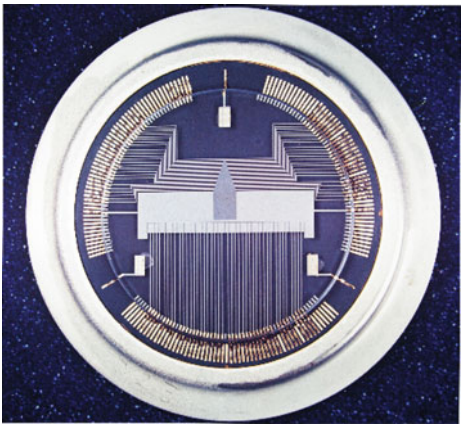

Figure 22.14: Discrete linear anode arrays of 1×48 pixels and 1×42 pixels used to measure the solar H Ly α line profile and intensity (see Kohl et al 1994). The 1×48 array is ≈ 3.3 mm long and the 1×42 array is ≈ 24 mm long (Ball Aerospace photograph).

A two-dimensional crossed-wire anode array has been developed for the *Einstein* (Giacconi et al 1979) and *AXAF* (now *Chandra*) (Weisskopf et al 2002) X-ray observatories, and has also been used on the *ROSAT* mission (Trümper 1984). Schematics of configuration of the High Resolution Imager (HRI), and of one dimension of the decoding scheme are shown in Figure 22.17 (Kellogg et al 1976). The performances of the HRI on *ROSAT* and on *Chandra* have been given, respectively, by Zombeck et al (1995), and by Murray et al (2000).

The characteristics of the *Chandra* HRI are a format of 1024×1024 pixels, a spatial resolution ≈ 20 µm FWHM (set by the MCP pore size), and a total output count rate > 150 s^{-1}. The most sophisticated analog MCP readout systems available today are the double delay line (DDL) and crossed delay line (XDL) (Siegmund et al 1993 and 1994), and the crossed strip (XS) detector (Siegmund et al 2001). XDL detectors with formats of 360×1024 pixels were flown in the UVCS and SUMER instruments on the *SOHO* mission (Siegmund et al 1994). Pixel dimensions were ≈ 25 µm FWHM and the global counting rates were stable to $> 4 \times 10^5$ s^{-1}. The XDL detectors were developed on an accelerated schedule because of the failure of the prime contractor to produce the MAMA detectors developed for these instruments (Timothy et al 1993). The XDL detectors performed well on UVCS. However, two problems occurred with the SUMER detectors because of the much higher signal levels and dynamic range. The first is the gain and dynamic range depression in the neighborhood of strong emission lines caused by the wide spread of the charge cloud from the Z stack MCP configuration (Wilhelm et al 1997). More seriously, the high gain ($\approx 10^7$) causes a relatively rapid gain sag with accumulated counts. Because the total charge that can be extracted from a lead glass MCP is limited, a detector requiring a gain of 10^8 will have a total count limit of about 100 times less than a detector requiring a gain of 10^6. On SUMER detector A operated for only about 200 days until the maximum voltage

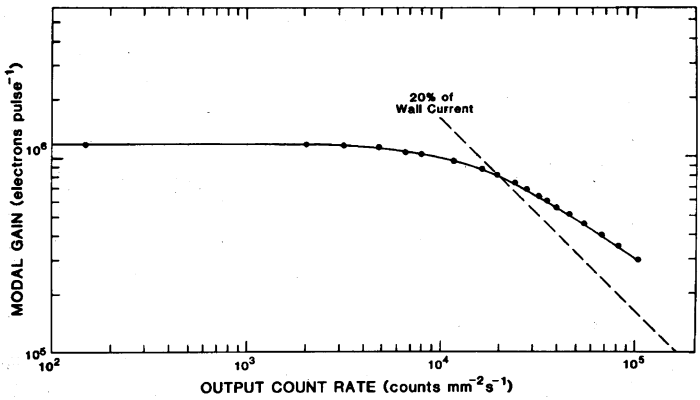

Figure 22.15: Modal gain as a function of count rate per unit area for a C-plate MCP with 25 µm channels, active area 25 mm in diameter and a resistance of 300 MΩ (from Timothy 1981).

of about 5400 V was reached. Detector B then operated for about 350 days before the maximum voltage was reached. Operation of both detectors continued for extended periods after the maximum voltage was reached, albeit with reduced photometric accuracy. Detector B is still operating as of this date. Details of the in-flight performance of the detectors have been presented by Griffiths et al (1998).

XDL arrays with formats of $\approx 2200 \times 2200$ resolution elements were also flown on the *GALEX* mission (Siegmund et al 1999). Two sealed detector tubes were used, one with an opaque CsI photocathode deposited on the MCP, and one with a semi-transparent photocathode deposited on the window. Many problems were encountered with the development and operation of the detectors because of the extreme cost and schedule constraints of the mission excellently described in detail by Morrissey (2006). On orbit the principal problems were transient overcurrent events that appeared to be closely correlated with active space weather (proton bursts and strong solar flares). A further problem associated with active space weather was the sudden appearance of a high-count rate "blob" which appeared in the FUV detector. The best explanation appears to be charging of the window that was held at a potential of about −5000 V. The FUV detector finally failed in June 2009 and the mission was arbitrarily terminated for fiscal reasons by NASA in 2011 with the NUV detector still operating.

Larger-format XDL arrays, optimized for spectroscopy, with $\approx 9000 \times 200$ resolution elements have been flown on the *FUSE* mission. These arrays employ longer helical DDL anodes deposited on two sides of a substrate (see Siegmund et al 1997). The two detectors, each with more than 9000×200 pixels, employ curved MCPs to match the focal surface of the spectrometer and are enclosed in a sealed detector body which can be opened for windowless operation. The MCPs are coated with an opaque KBr photocathode for maximum sensitivity in the 90.5 nm to 119 nm wavelength range. Operating windowless the *FUSE* detectors did not display most of the problems encountered with the *GALEX* detectors. Unexplained event bursts

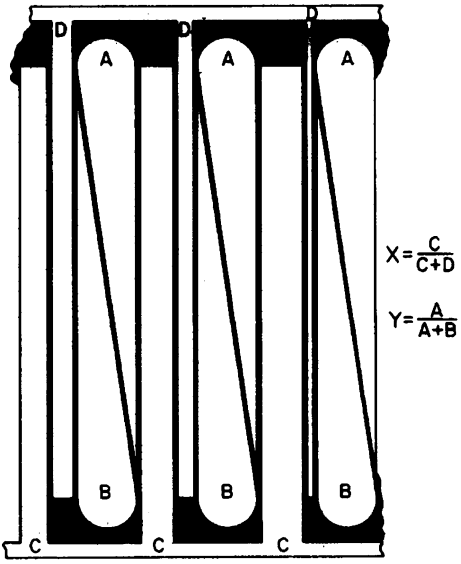

Figure 22.16: Four-electrode anode pattern for a WSA (from Martin et al 1981). Reproduced by permission of AIP.

were observed in all detector segments but appear to be of external nature and not caused by malfunctioning of the detectors. Gain sag was again a problem with the *FUSE* detectors (Sahnow 2003). The detectors were still operating well when the mission was terminated.

An upgraded version of the *FUSE* detector, the FUV detector in the Cosmic Origins Spectrograph (COS) instrument, was installed in the *HST* in May 2009 (McPhate et al 2000). This detector employs an opaque CsI photocathode for maximum sensitivity in the 115 nm to 177.5 nm spectral region. Like the *FUSE* detector the COS NUV detector is designed to operate windowless, maximizing the sensitivity. A highly desirable but bold decision given the uncertainties about the internal *HST* environment. Details of the final ground calibration have been presented by Vallerga et al (2001). The on-orbit performance has been good (McPhate et al 2010) with the exception of a short outage of about a month in 2012 caused by unexpected high count rates. However, yet again, gain sag has appeared as a problem. Gain sag in the analog XDL detectors is a serious problem, since it not only causes a loss of DQE in the highly exposed regions, but also degradation of imaging by "detector walk" (Sahnow et al 2011). Correction of the gain sag is now planned by moving the spectrum to a new location on the detector (Oliveira et al 2012).

Recognizing the problem of gain sag in the XDL detectors, cross-strip (XS) readout arrays have been developed by Siegmund et al (2001). The advantage of the XS array over the DDL and XDL arrays is the ability to operate at MCP gain levels $\approx 10^6$ rather than $> 10^7$, albeit with low global count rates ($\approx$10 kHz). New readout techniques with the potential for global count rates $\approx$1 MHz, have

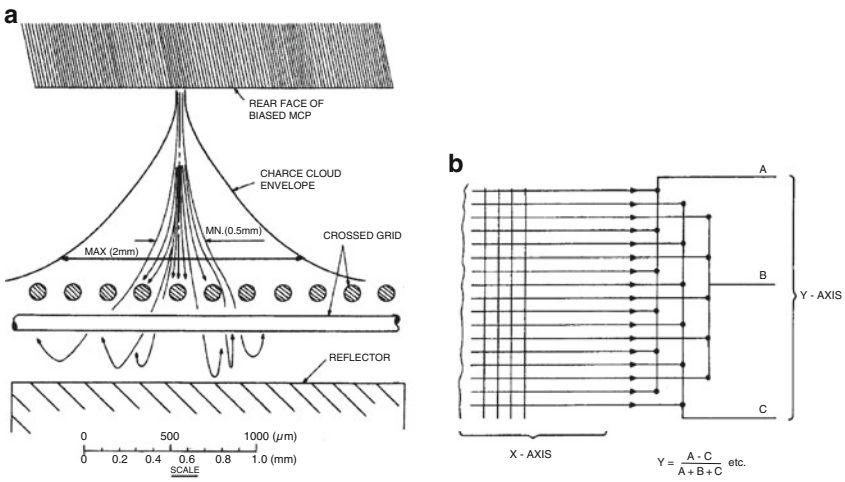

Figure 22.17: Schematics of the HRI readout system (from Kellogg et al 1976). a) Configuration of the two-dimensional array. b) Schematic of one dimension of the position encoding technique. Reproduced by permission of AIP.

been described by Tremsin et al (2006). The XS anode array employs a coarse (≈ 0.5 mm) multilayer metal and ceramic pattern that encodes event positions by direct sensing of the charge on each strip and determination of the charge cloud centroid for each event (see Figure 22.19). The XS detectors have yet to fly on a long-duration space mission.

The first class of digital readout arrays is the coded anode converter (CODACON). The simplified schematic of a one-dimensional CODACON readout array is shown in Figure 22.20. A charge pulse on a charge spreader causes charge to be induced in the code tracks. Differential amplifiers connected to each bit track pair determine which side of a pair has the most charge. The CODACON thus employs a 2^n encoding scheme where n is the number of code track pairs. Both one- and two-dimensional CODACONs have been built employing versions of Gray's binary code, as described by Lawrence and McClintock (1996) and the references therein. A 64×1024 pixel CODACON with a global count rate of 10^5 s^{-1} has been flown in the Ultraviolet Imaging Spectrograph on the *Cassini* mission to Saturn (McClintock et al 1993).

A light-weight ultraviolet imaging spectrograph has been developed for remote sensing of planetary atmospheres, based on the *Cassini* instrument and using a light-weight CODACON tube assembly together with FPGA electronics (McClintock and Lawrence 1996).

The second class of digital readout arrays is the multi-anode microchannel array (MAMA). The MAMA employs $2(n + 1)$ electrodes to uniquely define $n(n + 2)$ position locations in each axis. Thus $32 + 34$ electrodes uniquely define 32×34 or 1088 position locations. Details of the MAMA encoding scheme have been given by Slater et al (1990) and by Timothy (1994). The schematics of a coincidence-anode

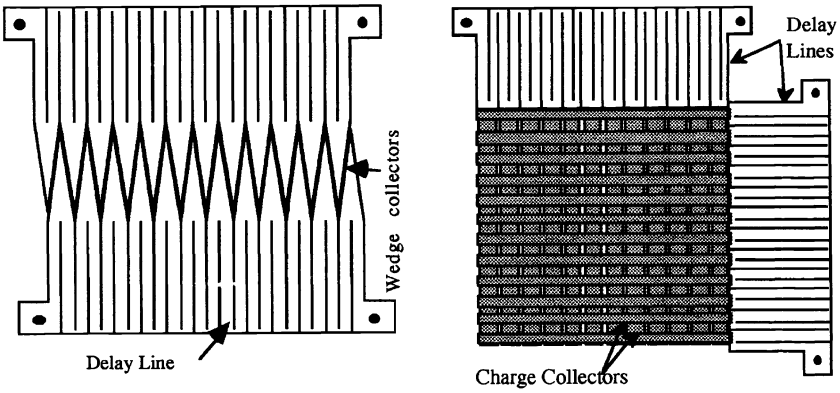

Figure 22.18: Schematics of DDL and XDL arrays (from Siegmund et al 1993). a) DDL anode with wedge charge collectors and external delay lines. b) XDL with external delay lines and crossed-finger charge collectors.

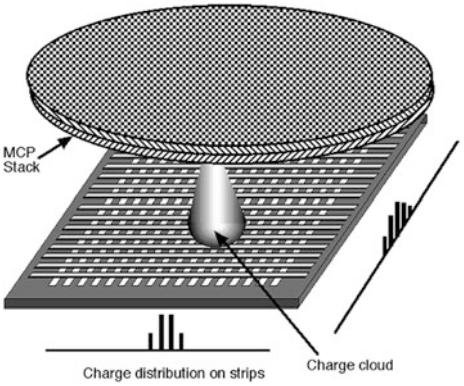

Figure 22.19: Schematic of XS anode array (from Siegmund et al 2001).

MAMA detector are shown in Figure 22.21. The simplified block diagram of a two-dimensional system is shown in Figure 22.21a, and the detection and encoding of multi-fold events, where the charge pulse stimulates two or more electrodes (the position of an event on a single electrode cannot be determined), is shown in Figure 22.21b.

The ability to discriminate between the detection of events on odd and even numbers of anode electrodes permits the spatial resolution to be doubled, as described by Kasle and Morgan (1991) and by Kasle and Horch (1992). The imaging MAMA detector designed for the STIS instrument on *HST* (see Figure 22.22) can accordingly be used as a 1024 × 1024 pixel array, or as a high-resolution 2048 × 2048 array. The spatial resolution is set by the pore size of the channels in the single C-plate MCP, namely 12 µm diameter channels on 15 µm centres.

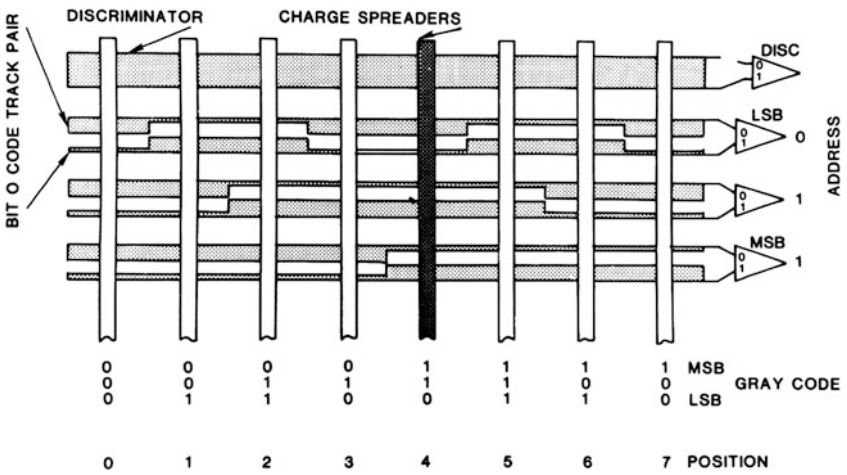

Figure 22.20: Simplified example of an eight-channel one-dimensional CODACON array (from McClintock et al 1982).

Two MAMA tubes are used in STIS; an NUV tube with a semi-transparent Cs-Te photocathode on an MgF_2 window, and an FUV tube with an opaque CsI photocathode and an MgF_2 window, see Figure 22.22, (Woodgate et al 1998). Details of the performances of these detectors have been given by Kimble et al (1998 and 1999). STIS was originally installed in *HST* in February 1997 during HSM2. STIS then operated normally until May 2001 when the Side-1 electronics failed. Operation was resumed in July 2001 using the redundant Side-2 electronics until August 2004 when the 5 V power supply failed. The detectors were undamaged and remained in a non-operating condition on orbit until STIS was repaired during HSM4 in May 2009. Considerable thought had to be given to the issues of bringing the MAMAs safely back into operation. The principal concern was migration of Cs in the NUV tube (and possibly also in the FUV tube) that could lead to an internal breakdown when high voltage was applied. The agreed approach was to very slowly raise the voltage at a rate that did not exceed the ohmic temperature rise of the MCP (about 15 min to full operating temperature). Further, the voltage was held at a level below the nominal operating voltage to permit a full analysis of the detector performance characteristics. Both detectors were successfully recovered. The dark count rate of the NUV detector was always higher than expected because of phosphorescent window glow arising from an error in the selection of the window material by the prime contractor. Prior to HSM4 the equilibrium dark count rate per pixel was 0.0013 s^{-1}. However, after the HSM4 recovery the dark count rate was as high as 0.015 s^{-1} with a much slower decay than expected. By late 2010 the dark count rate remained at about 0.0034 s^{-1} (Proffitt et al 2010). Further information has been presented by Zheng et al (2011). The dark count rate per pixel of the FUV detector has remained essentially constant at $\approx 10^{-5}$ s^{-1} at turn on. However, it gradually increases to as much as 6×10^{-4} s^{-1} because of the increase in the detector temperature during operation. An extra detector "glow" is then also observed,

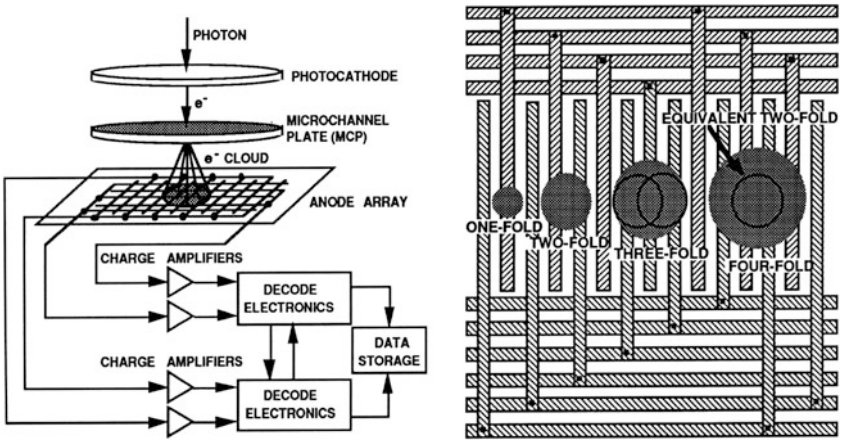

Figure 22.21: MAMA detector system schematics (from Kasle and Morgan 1991). Left: System block diagram. Right: One-dimensional fine-fine encoding scheme showing detection of multi-fold events.

being particularly strong in the upper left quadrant of the detector (http://www.stsci.edu/hst/HST_overview/documents). The STIS MAMA detectors have now been on orbit for well over 15 years and have been in continuous operation for nearly 11 years. At no time have the operating voltages of either detector needed to be changed to correct for gain sag or other detector issues (B Woodgate, personal communication).

In March 2002, during HSM3B, the STIS flight-spare FUV MAMA detector was installed on orbit in the Solar Blind Channel (SBC) of the Advanced Camera for Surveys (ACS) (see Chapter 5, Timothy et al 2013). The on-orbit performance was very similar to that of the STIS FUV detector, with an initial dark count rate per pixel of 1.049×10^{-5} s^{-1} (Tran et al 2002).

While the ACS suffered an electronics failure from January 2004 until the HSM4 repair in May 2009, the SBC remained in operation. At no time since 2002, in over 10.5 years of operation have the SBC FUV detector operating voltages required any changes and the SBC FUV detector remains in a nominal operating mode (http://www.stsci.edu/hst/HST_overview/documents).

Also during HSM4, the Cosmic Origins Spectrograph (COS) was installed on orbit. At the request of NASA the STIS flight-spare NUV MAMA detector was added to COS in order to provide a redundant capability for STIS. Because of better selection procedures for the window material the COS NUV detector is less noisy than the STIS NUV detector. Based on the window tests the initial dark count rate per pixel outside the SAA was predicted to be about 2.5×10^{-4} s^{-1} or about 25 % of the STIS values. However, the background count rate has continued to increase linearly, for unexplained reasons. The level as of February 2011 was about 4.3×10^{-4} s^{-1} and was predicted to rise to about 7.3×10^{-4} s^{-1} during Cycle 19 which ended in September 2012 (Sahnow et al 2011).

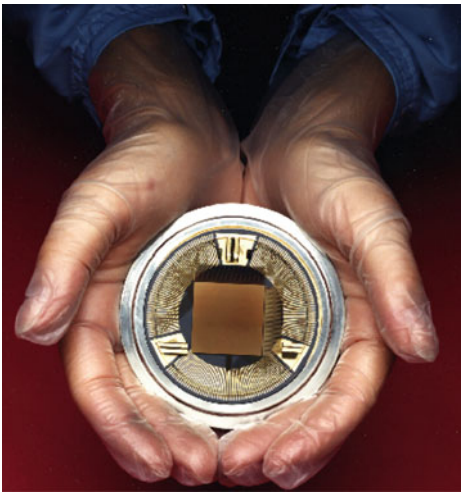

Figure 22.22: 1024 × 1024 pixel (2048 × 2048 pixel high resolution) MAMA array with 25 µm by 25 µm pixels (12.5 µm by 12.5 µm pixels high resolution) for the STIS instrument on *HST* (Ball Aerospace photograph).

It is of note that the four *HST* MAMAs have collectively accumulated over 28.5 years of on-orbit operation without requiring any changes in the operating voltages.

Fast timing and time-tag imaging

The transit time of electrons in a CEM or MCP depends linearly on the channel length, and the transit-time jitter is proportional to the transit time for a given applied voltage and length-to-diameter ratio (see Wiza 1979). CEMs and conventional PMTs typically produce pulses having a FWHM in the range from 5 ns to 30 ns. By comparison MCPs with channel diameters less than 12 µm produce pulses having an FWHM less than 1 ns. For example, a chevron MCP with 5 µm diameter channels produces a pulse width of order 0.5 ns (Laprade et al 1996, 1997). A 2 µm pore size MCP has been developed by Photonis USA. The measured pulse width is less than 400 ps (Laprade and Starcher 2001). This gives the MCP unique capabilities for fast timing applications, including time-of-flight (TOF) mass spectrometry (see, for example, Roman et al 2008). The result of this characteristic is that all of the electronic readout systems described here can record both the coordinates and the time of arrival of each detected photon to an accuracy set by the pulse-pair resolution of the electronics. This capability, which is unique to the MCP detectors, has a number of applications in space science. First, the integration time of the binned and time-tagged photons can be selected after the observations have been completed. Second, with a position reference, blurring of the image due to motion can be corrected. Third, frequency analyses of observed sources can be determined, and for pulsed sources the spectra of the different pulses can be selected

and analyzed. The examples given here are for the MAMA detector systems, but are equally applicable to all of the described systems. An example of the laboratory reconstruction of a moving image is shown in Figure 22.23.

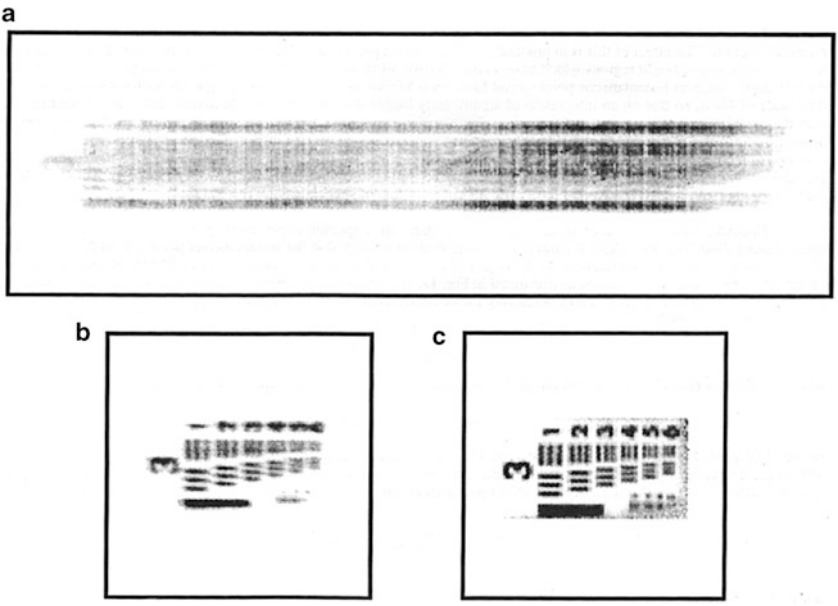

Figure 22.23: Image reconstruction of a moving image (from Giaretta et al 1993). a) Integrated image made from the raw time-tagged data of a portion of an Air Force test target while it was moving across the detector. b) Reconstructed image made by dividing the time-tagged data of the moving target into 0.1 s frames and centroiding each frame before co-adding. c) Flat-fielded image of the stationary Air Force target.

This technique was used to correct the jitter and gyro drift of a sounding rocket during FUV imagery of the galaxy NGC 6240 using a 256×1024 pixel MAMA detector system, by using star images within the field of view as references (Smith et al 1992). The raw and corrected images can be seen in Morgan et al (1990). An excellent example of the ability to select the optimum integration time with time-tag imaging is speckle interferometry, as described by Horch et al (1992). Some of the results of this technique are described by Horch et al (1999). The ultimate application for this technique is the ability to determine the spectra of the different pulses from a pulsed source. A specific example of this is the recording of the FUV spectra of the Crab pulsar pulses over the wavelength range from 160 nm to 320 nm using STIS (Gull et al 1998), as shown in Figure 22.24.

The future

Over 30 years ago conventional PMTs were considered, at best, obsolescent, and more likely obsolete. Yet today, thousands of these devices are in use. Similarly

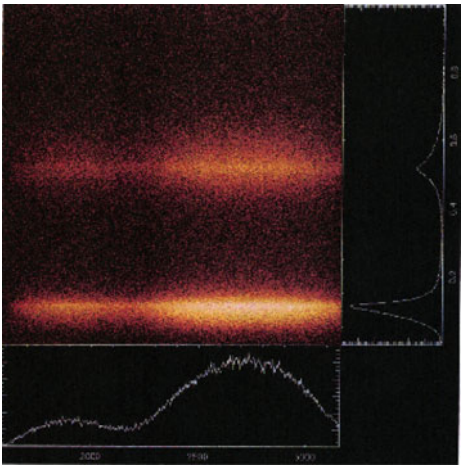

Figure 22.24: Crab pulsar profile spectra versus pulse phase from 160 nm to 320 nm (from Gull et al 1998). The data do not indicate any wavelength dependence of the pulse profile.

today, the major emphasis is on solid-state devices such as the CCDs and CMOS arrays, including the development of electron-multiplying CCDs with the goal of producing photon-counting arrays (see Chapter 23, Waltham 2013). However, the unique capabilities of MCPs and MCP stacks, plus their vast use in night-vision applications and particle detection (Wüest et al 2007), suggest that science-quality lead glass MCPs will be available for a long time to come.

The requirements for photon-counting, large-format detectors for future NASA UV astrophysics missions, particularly those devoted to spectroscopy, have been recently defined; specifically, arrays with high-QE (> 50 %), low noise per pixel ($< 10^{-7}$ s^{-1}), large-format ($> 2000 \times 2000$ pixels), operating at wavelengths from 100 nm to 400 nm or broader (`http://cor.gsfc.nasa.gov/technology/`).

Recent developments have attempted to find a superior MCP material than the lead-based glass, principally because of the conductivity limitations caused by the negative temperature coefficient of resistance. The development of silicon-based MCPs using lithographic techniques, which eliminate the multi-fiber spatial errors has been in progress for some time (see, for example, Siegmund et al 2004; Tremsin et al 2004). However it has not yet proved possible to obtain adequate gain from these MCPs, and the development of silicon MCPs does not appear to be actively pursued at this time. Developments to produce aluminum oxide MCPs are also under way at this time (Delendik et al 2003; Drobychev et al 2009). However, to date no working MCPs have been demonstrated.

Given the very high success rate in space of many different MCP detector systems over the past 25 years, it seems clear that the lead-glass MCPs have the capability of fully meeting the future requirements. This assumes that, for long-term space missions, it is possible to move the image or spectrum across the active area of the MCP in order to mitigate the effects of localized charge depletion by very

bright features. However, given the finite amount of charge that can be extracted from the lead glass, and the highly undesirable effects of very-high voltages in the space environment, an optimum MCP photon-counting detector system requires the following characteristics from the MCP:
1. A required gain of 10^6 or less.
2. A maximum operating voltage of 2000 V or less.
3. A single high-gain MCP, with highly effective suppression of ion feedback, to both improve the lifetime and to reduce the size of the charge cloud at the output.

In this regard, a recent development merits note. Namely, the production of the resistive and secondary emission layers by an atomic layer deposition (ALD) process (Ritala and Leskalä 1999). First, MCPs have been fabricated using hollow borosilicate tubes (Siegmund et al 2011). The tubes are then activated by an ALD process. Initial results are promising except for strong "chicken wire" effects at the multifiber boundaries. Second, nano-engineered conduction and emission layers have been deposited on conventional lead-glass MCPs (Beaulieu et al 2009, see also `www.arradiance.com`). The initial results appear highly promising.

The most critical development area is that of producing stable high quantum efficiency solar-blind photocathode materials. Currently the most efficient photocathode materials for use at wavelengths below about 150 nm are opaque alkali halides (CsI, KBr, and NaBr) (see, for example, Siegmund et al 2007). These photocathodes must be protected from the ambient atmosphere, but can be operated stably in the open-structure mode in space.

One material that currently shows great promise is p-doped GaN (Norton et al 2003; Dabiran et al 2009; Siegmund et al 2010; Ainbund et al 2012). These negative-affinity photocathodes have very low sensitivity above about 350 nm and, in an opaque form, a high QE at wavelengths below about 300 nm. They also appear to be stable with time.

A number of MCP detector systems with different readout systems are now under development for future space missions (see, for example, Wilkinson et al 2012; Diebold et al 2012; Uslenghi et al 2012).

Whatever the results of these developments, there will always be a requirement in UV and X-ray astrophysics instruments for solar-blind, photon-counting imaging detector systems, which are radiation tolerant and which do not require cryogenic cooling.

Notes

The references to commercial organizations in this chapter are for technical purposes only and do not represent any endorsement on the part of the author, the editors, or the publisher.

References

Adams J, Manley BW (1966) The mechanism of channel electron multiplication. IEEE Trans Nucl Sci NS-13:88–99

Ainbund MR, Alekseev AN, Alymov OV (plus six authors) (2012) Solar-blind UV photocathodes based on AlGaN heterostructures with a 300 to 350 nm spectral sensitivity threshold. Techn Phys Lett 38:439–442

Beaulieu DR, Gorelikov D, de Rouffignac P (plus four authors) (2009) Nano-engineered ultra high gain microchannel plates. Nucl Instr Meth Phys A 607:81–84

Blodgett KB (1951) Surface conductivity of lead silicate glass after hydrogen treatment. J Am Ceram Soc 34:14–27

Boutot JP, Eschard G, Polaert R, Duchenois V (1974) A microchannel plate with curved channels: an improvement in gain, relative variance and ion noise for channel plate tubes. Proc of Sixth Symposium on Photo-electronic Image Devices, London, pp 103–111

Breeveld AA, Edgar ML, Smith A (plus two authors) (1992) A SPAN MCP detector for the *SOHO* Coronal Diagnostics Spectrometer. Rev Sci Instrum 63:673–676

Clampin M, Paresce F (1989) Photon-counting imaging with a GaAs photocathode: evaluation of the Red-RANICON for astronomical imaging. Astron Astrophys 225:578–584

Corbett MB, Feller WB, Laprade BN (plus four authors) (1992) Development Efforts to Improve Curved-channel Microchannel Plates. Proc SPIE 1764:240–251

Csorba IP (1980) Current gain parameters of microchannel plates. Appl Opt 19:3863–3866

Csorba IP (1985a) Phosphor screens, in image tubes. Howard W Sams & Co, Inc, (Publishing Subsidiary of ITT), 29–42

Csorba IP (1985b) Image intensifier tube types, in Image Tubes, Howard W Sams & Co, Inc, (Publishing Subsidiary of ITT), 174–193

Dabiran AM, Wowchak AM, Chow PP (plus four authors) (2009) Direct deposition of GaN photocathodes on microchannel plates. Proc SPIE 7212:721213-1–721213-6

De Korte PAJ, Bleeker JAM, den Boggende AJF (plus six authors) (1981) The X-ray imaging telescopes on *EXOSAT*. Space Sci Rev 30:495–511

Delendik K, Emeliantchik I, Litomin A (plus two authors) (2003) Aluminum oxide microchannel plates. Nucl Phys B 125:394–399

Diebold S, Barnstedt J, Elsener H-R (plus nine authors) (2012) MCP detector development for WSO-UV. Proc SPIE 8443:84432X-1–84432X-8

Drobychev G, Barysevich A, Delendik K (plus four authors) (2007) Development of micro-channel plates on the basis of aluminum oxide. Nucl Instr Meth A 567:290–293

Drobychev G, Barysevich A, Delendik K (plus three authors) (2009) Advances in anodic Alumina MCP development. Nucl Inst Meth Phys A 610:246–248

Evans DS (1965) Low energy charged-particle detection using the continuous-channel electron multiplier. Rev Sci Instrum 36:375–382

Eschard G, Manley BW (1971) Principles and characteristics of channel electron multipliers. Acta Electronica 14:19–39

Farnsworth PT (1930) Electron multiplier, US Patent number 1 969 399

Giacconi R, Branduardi G, Briel U (plus 28 authors) The *Einstein (HEAO 2)* X-ray observatory. Astrophys J 230:540–550

Giaretta G, Horch E, Timothy JG, Heanue JF (1993) Time-tag photon detection with the MAMA detector system. Proc SPIE 1952:316–328
Goodrich GW, Wiley WC (1962) Continuous channel electron multiplier. Rev Sci Instrum 33:761–762
Griffiths NW, Airieau S, Siegmund OHW (1998) In-flight performance of the SUMER microchannel plate detectors. Proc SPIE 3446:566–577
Guest AJ (1971) A computer model of channel multiplier plate performance. Acta Electronica 14:79–97
Gull TR, Lindler DJ, Crenshaw DM (plus eight authors) (1998) Space telescope imaging spectrograph near-ultraviolet time-tagged spectra of the Crab pulsar. Astrophys J 495:L51–54
Heroux L, Hinteregger HE (1960) Resistance strip magnetic electron multiplier for the extreme ultraviolet. Rev Sci Instrum 31:280–286
Horch E, Morgan JS, Giaretta G, Kasle DB (1992), A new speckle interferometry system for the MAMA detector. Pub Astron Soc Pacific 104:939–948
Horch E, Ninkov Z, van Altena WF (plus three authors) (1999) Speckle observations of binary stars with the WIYN telescope I. Measures during 1997. Astronom J 117:548–561
Kasle DB, Morgan JS (1991) High resolution decoding of multi-anode microchannel array detectors. Proc SPIE 1549:52–58
Kasle DB, Horch EP (1992) Performance of high resolution decoding with multi-anode microchannel array detectors. Proc SPIE 1764:202–216
Kellogg E, Henry P, Murray S, Van Speybroek L (1976), High-resolution imaging X-ray detector. Rev Sci Instrum 47:282–290
Kimble RA, Woodgate BE, Bowers C (plus 50 authors) (1998) The on-orbit performance of the Space Telescope Imaging Spectrograph, Proc SPIE 3356:188–202
Kimble RA, Abraham J, Argebright VS (plus 15 authors) (1999) In-flight performance of the MAMA detectors on the Space Telescope Imaging Spectrograph. Proc SPIE 3764:209–225
Kohl JL, Gardner LD, Strachan L, Hassler DM (1994) Ultraviolet spectroscopy of the extended solar corona during the *SPARTAN* 201 Mission. Space Sci Rev 70:253–261
Lampton M, Paresce F (1974) The Ranicon: A resistive anode image converter. Rev Sci Instrum 45:1098–1105
Lampton M, Carlson CW (1979) Low-distortion resistive anodes for two-dimensional position-sensitive MCP systems. Rev Sci Instrum 50:1093–1097
Laprade B, Dykstra M, Langevin F (1996) The development of an ultra small pore microchannel plate for space sciences applications. (1996) Proc SPIE 2808:72–85
Laprade B, Cochran RC, Langevin F, Dykstra MW (1997) Characterization of an ultra small pore microchannel plate. Proc SPIE 3173:474–485
Laprade B, Starcher R (2001) The 2 micron pore microchannel plate. Photonis USA, Sturbridge MA
Lawrence GM, McClintock WE (1996) Compact ultraviolet imaging microchannel plate detectors using CODed Anode Convertor (CODACON) readout systems. Proc SPIE 2831: 104–111
Macar PJ, Rechavi J, Huber MCE, Reeves EM (1970) Solar-blind photoelectric detection systems for satellite applications. Appl Opt 9:581–593

Martin C, Jelinsky P, Lampton M, Malina RF (1981) Wedge-and-strip anodes for centroid position sensitive photon and particle detectors. Rev Sci Instrum 52:1067–1074

Mason IM, Braduardi-Raymont G, Culhane JL (plus three authors) The *EXOSAT* imaging X-ray detectors. (1984) IEEE Trans Nucl Sci NS-31:795–800

McClintock WE, Barth CA, Steele RE (plus two authors) (1982) Rocket-borne instrument with a high resolution microchannel plate detector for planetary UV astronomy. Appl Opt 21:3071–3079

McClintock WE, Lawrence GM, Kohnert RA, Esposito LW (1993) Optical design of the Ultraviolet Imaging Spectrograph for the *Cassini* mission to Saturn. Opt Engineering 32:3038–3046

McClintock WE, Lawrence GM (1996) Low-mass, Low-power Ultraviolet Telescope-Imaging Spectrograph for Planetary Atmosphere Remote Sensing. Proc SPIE 2807:256–266

McPhate JB, Siegmund OH, Gaines G (plus two authors) (2000) The Cosmic Origins Spectrograph FUV detector. Proc SPIE 4139:25–33

McPhate JB, Siegmund OH, Vallerga JV (plus eight authors) (2010) *Hubble* Space Telescope: Cosmic Origins Spectrograph FUV detector initial on-orbit performance. Proc SPIE 77322H, pp 7

Morgan JS, Timothy JG, Smith AM (plus two authors) (1990) High time-resolution imaging with the MAMA detector systems, Proc SPIE 1235:347–357

Morrissey P (2006) A *GALEX* instrument overview and lessons learned. Proc SPIE 6266:62660Y1-15

Murray SS, Austin GK, Chappell JH (plus seven authors) (2000) In-flight performance of the *Chandra* High Resolution Camera. Proc SPIE 4012:68–80

Norton TJ, Woodgate BE, Stock J (plus four authors) (2003) Results from Cs activated GaN photocathode development for MCP detector systems at NASA GSFC. Proc SPIE 5164:155–164

Oliveira CM, Aloisi A, Ely J (plus seven authors) (2012) A fresh start for the COS FUV detector. Amer Astron Soc Meeting 220, 136.03

Oschepkov PK, Skvortsov BN, Osanov BA, Sibrikov I (1960) Application of a continuous secondary electron multiplication for amplifying small currents (Translation). Pribory Tekh Eksper 4:89–91

Piore ER, Harvey GG, Gyorgy EM, Kingston RH (1952) A high vacuum recording spectrograph for the study of radiation from solids in the 100–800 Å range. Rev Sci Instrum 23:8–12

Proffitt CR, Aloisi A, Bohlin RC (plus 16 authors) (2010) Performance of the Space Telescope Imaging Spectrograph after SM4. The 2010 STScI Calibration Workshop: 47–56

Reeves EM, Huber MCE, Timothy JG (1977) Extreme UV spectroheliometer on the Apollo Telescope Mount. Appl Opt 16:837–857

Ritala M and Leskalä M (1999) Atomic layer epitaxy – a valuable tool for nanotechnology? Nanotechnology 10:19

Roman PA, Brickerhoff WB, Getty SA (plus five authors) (2008) A miniature MEMS and NEMS enabled time-of-flight mass spectrometer for investigations in planetary science. Proc SPIE 6959:6959G-1–13

Sahnow DJ (2003) The FUSE detectors: on orbit use and lessons learned. Proc SPIE 4854:610–619
Sahnow DJ, Oliviera C, Aloisi A (plus ten authors) (2011) Gain sag in the FUV detector of the Cosmic Origins Spectrograph. Proc SPIE 8145:poster session
Sahnow D, Ake T, Penton S (plus two authors) (2011) COS NUV detector dark rates during SMOV and Cycle 17. STScI Instrument Science Report COS 2010-12
Schühle U (2013) Intensified solid state sensor cameras: ICCD and IAPS. ISSI SR-009:455–465
Siegmund OHW, Malina RF, Coburn K, Werthimer D (1984) Microchannel plate EUV detectors for the Extreme Ultraviolet Explorer. IEEE Trans Nucl Sci NS-31:776–779
Siegmund OHW, Coburn K, Malina RF (1985) Investigation of large format microchannel plate Z configurations. IEEE Trans Nucl Sci NS-32:443–447
Siegmund OHW, Lampton M, Bixler J (plus two authors) (1986) Operational characteristics of wedge and strip readout systems. IEEE Trans Nucl Sci 33:724–727
Siegmund OHW, Everman E, Vallerga JV (plus two authors) (1987) Ultraviolet quantum detection efficiency of potassium bromide as an opaque photocathode applied to microchannel plates. Appl Opt 26:3607–3614
Siegmund OHW, Cully SL, Gaines GA (plus three authors) (1990) Highly curved microchannel plates, EUV, X-ray and Gamma-ray instrumentation for astronomy. Proc SPIE 1344:346–354
Siegmund OHW, Gummin M, Stock J (plus three authors) (1993) High resolution monolithic delay line readout techniques for two dimensional microchannel plate detectors. Proc SPIE 2006:176–186
Siegmund OHW, Gummin M, Stock J (plus ten authors) (1997) Performance of the double delay line microchannel plate detectors for the Far Ultraviolet Spectroscopic Explorer. Proc SPIE 3114:283–294
Siegmund OHW, Stock JM, Marsh DR (plus 17 authors) (1994) Delay line detectors for the UVCS and SUMER instruments on the *SOHO* satellite, EUV, X-ray, and Gamma-ray instrumentation for astronomy. Proc SPIE 2280:89–100
Siegmund OHW, Gummin MA, Sasseen T (plus eight authors) (1995) Microchannel Plates for the UVCS and SUMER instruments on the *SOHO* satellite. Proc SPIE 2518:344–355
Siegmund OHW, Jelinsky P, Jelinsky S (plus six authors) (1999) High-resolution cross delay line detectors for the GALEX mission. Proc SPIE 3765:429–440
Siegmund OHW, Tremsin AS, Vallerga JV, Hull J (2001) Cross strip imaging anodes for microchannel plate detectors. IEEE Trans Nucl Sci 48:430–434
Siegmund OHW, Vallerga JV, McPhate J, Tremsin AS (2004) Next generation microchannel plate detector technologies for UV Astronomy. Proc SPIE 5488:789–800
Siegmund OHW, Vallerga J, Tremsin A, McPhate J (2007) Microchannel plates: Recent advances in performance. Proc SPIE 6686, web reference 66860W
Siegmund OHW, Hall JS, Tremsin AS (plus two authors) (2010) Gallium nitride photocathodes for imaging photon counters. Proc SPIE 7732:4T-1–9

Siegmund OHW, Fujiwara K, Hemphill R (plus 13 authors) (2011) Advances in microchannel plates and photocathodes for ultraviolet photon counting detectors. Proc SPIE 8145:81450J-1–12

Slater DC, Timothy JG, Morgan JS, Kasle DB (1990) Imaging MAMA Detector Systems. Proc SPIE 1243:35–49

Smith AM, Hill RS, Vrba FJ, Timothy JG (1992) Far-ultraviolet MAMA detector imagery and emission-line CCD imagery of NGC 6240. Astrophys J 391:L81–84

Sommer AH, Photoemissive Materials (1980) Robert E Krieger Publishing Company, Huntington, New York

Spicer WE (1975) Negative electron affinity photocathode research and technology. IEEE Electron Devices 21:57–59

Timothy AF, Timothy JG, Willmore AP (1967) The performance of open structure photomultipliers in the 1100-Å to 250-Å wavelength region. Appl Opt 6:1319–1326

Timothy JG, Bybee RL (1977a) Preliminary results with microchannel plates employing curved microchannels to inhibit ion feedback. Rev Sci Instrum 48:292–299

Timothy JG, Bybee RL (1977b), Multi-anode microchannel arrays. Proc SPIE 116:24–32

Timothy JG, Lapson LB (1974) Use of channel electron multipliers as secondary standard detectors at EUV wavelengths. Appl Opt 13:1417–1430

Timothy JG, Reeves EM, Chambers RM (plus two authors) (1975) A sounding rocket spectroheliometer for photometric studies at extreme ultraviolet wavelengths. Space Sci Instrum 1:23–49

Timothy JG (1981) Curved-channel microchannel array plates. Rev Sci Instrum 52:1131–1142

Timothy JG, Bergamini P, Berger TE (plus two authors) (1993) Performance characteristics of the MAMA detectors for the SUMER instrument on the *SOHO* Mission. Proc SPIE 2006:69–76

Timothy JG (1994) Recent advances with the MAMA detector systems. Proc SPIE 2278:134–137

Timothy JG, Wilhelm K, Xia L (2013) The extra-terrestrial vacuum-ultraviolet wavelength range. ISSI SR-009:93–120

Tran HD, Meurer G, Ford HC (plus nine authors) (2002) On-orbit performance of the ACS solar blind channel. STScI 2002 Calibration Workshop:86–89

Tremsin AS, Vallerga JV, Siegmund OHW (plus two authors) (2004) Thermal dependence of electrical characteristics of micromachined silica microchannel plates. Rev Sci Instr 75:1068–1072

Tremsin AS, Siegmund OHW (2005) The quantum efficiency and stability of UV and soft X-ray photocathodes. Proc SPIE 5920:1–13

Tremsin AS, Siegmund OHW, Vallerga JV, Hull JS (2006) Novel high resolution readout for UV and X-ray photon counting detectors with microchannel plates. Proc SPIE 6276:627616-1–627616-11

Trümper J (1984) *ROSAT*. Physica Scripta T7:209–215

Uslenghi M, Incorvaia S, Fiorini M (2012) (plus 11 authors) A prototype of the UV detector for MATIS on *Solar Orbiter*. Proc SPIE 8443:84433I-1–84433I-9

Vallerga JV, Eckert M, Sirk M (1994) (plus two authors) Long-term orbital performance of the MCP detectors aboard the Extreme Ultraviolet Explorer. Proc SPIE 2280:57–68

Vallerga J, McPhate J, Martin A (plus five authors) (2001) The *HST*-COS Far Ultraviolet Detector: Final ground calibration. Proc SPIE 4498:141–151

Waltham N (2013) CCD and CMOS sensors. ISSI SR-009:423–442

Washington D (1971) Improvements in or relating to Electron Multipliers. UK Patent 1352732

Washington D, Duchenois V, Polaert R, Beasley RM (1971) Technology of channel plate manufacture. Acta Electronica 14:201–224

Weisskopf MC, Brinkman B, Canizares C (plus three authors) (2002) An overview of the performance and scientific results from the *Chandra* X-Ray observatory. Publ Astron Soc Pacific 114:1–24

Wiley WC, Hendee CF (1962) Electron multipliers utilizing continuous strip surfaces. IRE Trans Nucl Sci NS-9:103–106

Wilhelm K, Lemaire P, Curdt W (plus 16 authors) (1997) First Results of the SUMER Telescope and Spectrometer on *SOHO*; I. Spectra and Spectroradiometry. Sol Phys 170:75–104

Wilkinson E, Vincent M, Kofoed C (plus three authors) (2012) Southwest Research Institute intensified detector development capability. Proc SPIE 8443:84432K-1–84432K-7

Wiza JL (1979) Microchannel plate detectors. Nucl Instrum Meth 162:587–601

Woodgate BE, Kimble RA, Bowers CW (plus 41 authors) (1998) The Space Telescope Imaging Spectrograph design. PASP 110:1183–1204

Wuest M, Evans DS, McFadden JP (plus seven authors) (2007) Review of instruments. ISSI SR-007:11–101

Young AT (1974) Photomultipliers: Their cause and cure, in Methods of Experimental Physics 12 (ed. N Carleton) Academic Press, New York and London, 1–94

Zheng W, Proffitt C, Sahnow D (2011) Dark rate of the STIS NUV detector. STScI Instrument Science Report STIS 2011-03

Zombeck MV, David LP, Harnden FR Jr, Kearns K (1995) Orbital performance of the high resolution imager on *ROSAT*. Proc SPIE 2518:304–320